Journal of Biomechanics 80 (2018) 179–185

Contents lists available at ScienceDirect

Journal of Biomechanics

journal homepage: www.elsevier.com/locate/jbiomech
www.JBiomech.com

Short communication

A fiduciary marker-based framework to assess heterogeneity and anisotropy of right ventricular epicardial strains in the beating ovine heart

William D. Meador [a,b], Marcin Malinowski [c,d], Tomasz Jazwiec [c], Matthew Goehler [c], Nathan Quay [c], Tomasz A. Timek [c], Manuel K. Rausch [a,b,e,*]

[a] Department of Aerospace Engineering and Engineering Mechanics, University of Texas at Austin, TX, USA
[b] Department of Biomedical Engineering, University of Texas at Austin, TX, USA
[c] Meijer Heart and Vascular Institute at Spectrum Health, Michigan, MI, USA
[d] Department of Cardiac Surgery, Medical University of Silesia, Katowice, Poland
[e] Institute for Computational Engineering and Sciences, University of Texas at Austin, TX, USA

ARTICLE INFO

Article history:
Accepted 31 August 2018

Keywords:
Cardiovascular
Myocardium
Kinematics
Sonomicrometry
Subdivision surface

ABSTRACT

Quantifying ventricular deformation in health and disease is critical to our understanding of normal heart function, heart disease mechanisms, and the effect of medical treatments. Imaging modalities have been developed that can measure ventricular deformation non-invasively. However, because of the small thickness, complex shape, and anatomic position of the right ventricle, using these technologies to determine its deformation remains challenging. Here we develop a first fiduciary marker-based method to assess heterogeneity and anisotropy of right ventricular epicardial strain across the entire free wall. To this end, we combine a high-density array of sonomicrometry crystals implanted across the entire right ventricular epicardial surface with a subdivision surface algorithm and a large deformation kinematics framework. We demonstrate our approach on four beating ovine hearts and present a preliminary regional analysis of circumferential, longitudinal, and areal strain. Moreover, we illustrate maps of the same strains across the entire right ventricular epicardial surface to highlight their spatial heterogeneity and anisotropy. We observe in these animals that RV epicardial strains vary throughout the cardiac cycle, are heterogeneous across the RV free wall, and are anisotropic with larger compressive strains, i.e., contraction, in the longitudinal direction than in the circumferential direction. Average peak compressive strains vary by region between −3.34% and −8.29% in circumferential direction, and −4.02% and −10.57% in longitudinal direction. In summary, we introduce an experimental framework that will allow us to study disease- and device-induced deformations, and long-term consequences of these deformations, including heterogeneous and anisotropic effects.

1. Introduction

Quantifying normal right ventricular (RV) deformation is critical to our understanding of RV function. It may also provide insights into mechanisms of RV diseases, such as right heart failure (Voelkel et al., 2006). To date there is a number of non-invasive imaging modalities that allow assessing ventricular function in patients, such as tagged MRI (Lee et al., 2011; Yeon et al., 2001) and DENSE MRI (Zhang et al., 2017; Zhong et al., 2010), Tissue Doppler Echocardiography and Speckle Tracking Echocardiography (Bleeker, 2006; La Gerche et al., 2010), and 3D Echocardiography (Zhang et al., 2013). However, quantifying RV deformation non-invasively can be challenging because of the RV's complex geometry, thin wall, and anatomic position (Haddad et al., 2008; Ho and Nihoyannopoulos, 2006). Moreover, none of the above methods employ fiduciary markers, which ensure accurate tracking of specific material points and allow to quantify strains between configurations with large temporal separation, i.e., tracking of deformations that occur over periods longer than a few cardiac cycles. Therefore, these imaging techniques are not ideal for assessing disease- and device-induced deformations (Genet et al., 2015; Kroon et al., 2009; Lee et al., 2016).

* Corresponding author at: 210 E 24th Street, WRW Building, Room 305b, Austin, TX 78712, USA.
E-mail address: manuel.rausch@utexas.edu (M.K. Rausch).

https://doi.org/10.1016/j.jbiomech.2018.08.036
0021-9290/

To overcome these challenges, in this current study, we demonstrate the feasibility of a sonomicrometry-based experimental technique to study heterogeneous and anisotropic RV epicardial strains in an ovine model.

2. Materials and methods

2.1. Surgical procedure and experimental protocol

We perform the following surgical procedure and experimental protocol according to the Principles of Laboratory Animal Care, which was formulated by the National Society for Medical Research, and the Guide for Care and Use of Laboratory Animals prepared by the National Academy of Science and published by the National Institutes of Health. Furthermore, this protocol was approved by our local Institutional Animal Care and Use Committee (IACUC #: 17-05).

We described the animal procedure and all administered medications in detail previously (Malinowski et al., 2016b, 2016a; Rausch et al., 2017b). Briefly, we pre-medicate four healthy, male sheep (47 ± 4 kg), anesthetize them intravenously, intubate and mechanically ventilate them, and maintain anesthesia. We catheterize the jugular vein and the carotid artery for central venous and arterial access, respectively, before we perform a median sternotomy and prepare the heart for cardiopulmonary bypass. Once on bypass, while the heart is beating, we place pressure sensors in the RV and left ventricle (LV) via the apex. Next, we surgically implant 20 sonomicrometry crystals on the RV epicardium, spanning the entire free wall (Fig. 1). Following placement of pressure sensors and sonomicrometry crystals, we collect crystal position data at 128 Hz sampling frequency under open chest, open pericardium conditions. At the end of the experiment, we euthanize all animals.

2.2. Ventricular strain calculations

To calculate RV epicardial strain in the beating ovine heart we use an approach we previously described (Rausch et al., 2012, 2011). Specifically, we manually create a triangular connectivity list between the sonomicrometry-derived crystal coordinates and subsequently interpolate each triangular element via linear shape functions in terms of the local curvilinear coordinates θ^α, with $\alpha = 1,2$. Thus, we only characterize the *surface* deformations of the RV. We describe the reference coordinates $\boldsymbol{X}(\theta^1,\theta^2)$ and spatial coordinates$\boldsymbol{x}(\theta^1,\theta^2)$ of the RV epicardial surface for each animal as per

$$\boldsymbol{X}(\theta^1,\theta^2)=\sum_{I=1}^{n} N_I(\theta^1,\theta^2)\boldsymbol{X}_I,\ \text{ and }\ \boldsymbol{x}(\theta^1,\theta^2)=\sum_{I=1}^{n} N_I(\theta^1,\theta^2)\boldsymbol{x}_I, \tag{1}$$

respectively, where $N_I(\theta^1,\theta^2)$ are aforementioned linear shape functions, and $\boldsymbol{X}_I$ and $\boldsymbol{x}_I$ are the crystal positions in the reference configuration and spatial configuration. Based on the partial derivatives of the shape functions, we next compute covariant base vectors in both configurations,

$$\boldsymbol{G}_\alpha(\theta^1,\theta^2)=\sum_{I=1}^{n} \partial N_I/\partial\theta^\alpha \boldsymbol{X}_I,\ \text{ and }\ \boldsymbol{g}_\alpha(\theta^1,\theta^2)=\sum_{I=1}^{n} \partial N_I/\partial\theta^\alpha \boldsymbol{x}_I \tag{2}$$

We determine the contravariant counterparts to the above bases via the covariant surface metric in the reference configuration $G_{\alpha\beta}=\boldsymbol{G}_\alpha\cdot\boldsymbol{G}_\beta$, viz.,

$$\boldsymbol{G}^\alpha = G^{\alpha\beta}\boldsymbol{G}_\beta,\ \text{ where }\ G^{\alpha\beta}={G_{\alpha\beta}}^{-1},\ \text{ with }\ \alpha,\beta=1,2 \tag{3}$$

and via the covariant surface metric in the current configuration $g_{\alpha\beta}=\boldsymbol{g}_\alpha\cdot\boldsymbol{g}_\beta$, viz.,

$$\boldsymbol{g}^\alpha = g^{\alpha\beta}\boldsymbol{g}_\beta,\ \text{ where }\ g^{\alpha\beta}={g_{\alpha\beta}}^{-1} \tag{4}$$

Additionally, we can compute the Green-Lagrange strain tensor as

$$\boldsymbol{E}=E_{\alpha\beta}\boldsymbol{G}^\alpha\otimes\boldsymbol{G}^\beta,\ \text{ where }\ E_{\alpha\beta}=\frac{1}{2}\left[g_{\alpha\beta}-G_{\alpha\beta}\right]. \tag{5}$$

We compute the circumferential and longitudinal strains, E_c and E_l, as the projections of the Green-Lagrange strain tensor onto the circumferential and longitudinal direction vectors, $\boldsymbol{n}_c$ and $\boldsymbol{n}_l$, respectively, which we determine for each triangular element, i.e.,

$$E_c=\boldsymbol{n}_c\cdot\boldsymbol{E}\cdot\boldsymbol{n}_c,\ \text{ and }\ E_l=\boldsymbol{n}_l\cdot\boldsymbol{E}\cdot\boldsymbol{n}_l. \tag{6}$$

Specifically, for each triangular element, we calculate $\boldsymbol{n}_l$ as the vector connecting the triangular element's centroid with the apical crystal, projected onto the triangular element's surface. Subsequently the result is normalized. We calculate the circumferential direction vector $\boldsymbol{n}_c$ as the cross-product between $\boldsymbol{n}_l$ and the triangular element's outward normal vector (Fig. 1).

Finally, we compute areal strain, E_a, as the relative change in each triangular element's surface area between the current and the reference configuration.

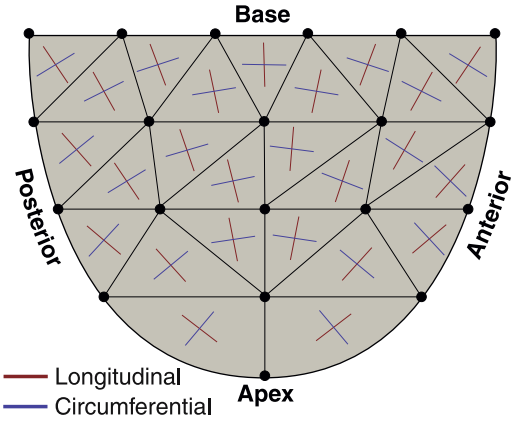

Fig. 1. Sonomicrometry crystal placement across the right ventricular epicardial surface with triangular connectivity. In total, we implanted 20 crystals to create a triangular mesh of 25 elements. Vectors indicate the approximate circumferential (blue) and longitudinal (red) directions for each element. (For interpretation of the references to color in this figure legend, the reader is referred to the web version of this article.)

2.3. Smooth right ventricular epicardial surface representation

To recreate smooth surface representations of the RV epicardial surfaces, we use the Loop subdivision scheme (Cirak et al., 2000; Göktepe et al., 2010; Loop, 1987). Generally, approximating subdivision schemes create surfaces that are off-set from the original control mesh. To circumvent this obvious shortcoming, we subsequently employ an augmented fixed point method (Rausch et al., 2017a). To this end, we perform three iterations of the Loop subdivision algorithm to obtain an approximating, C^2-continuous RV epicardial surface. Next, we calculate an error vector between each crystal and the closest subdivision surface point. Subsequently, we iteratively displace each original control mesh node by their respective scaled error vectors and re-compute a new smooth surface based on this updated control mesh (Fig. 2).

3. Results

All four subjects included in our study recovered well from bypass with normal hemodynamics (Table 1).

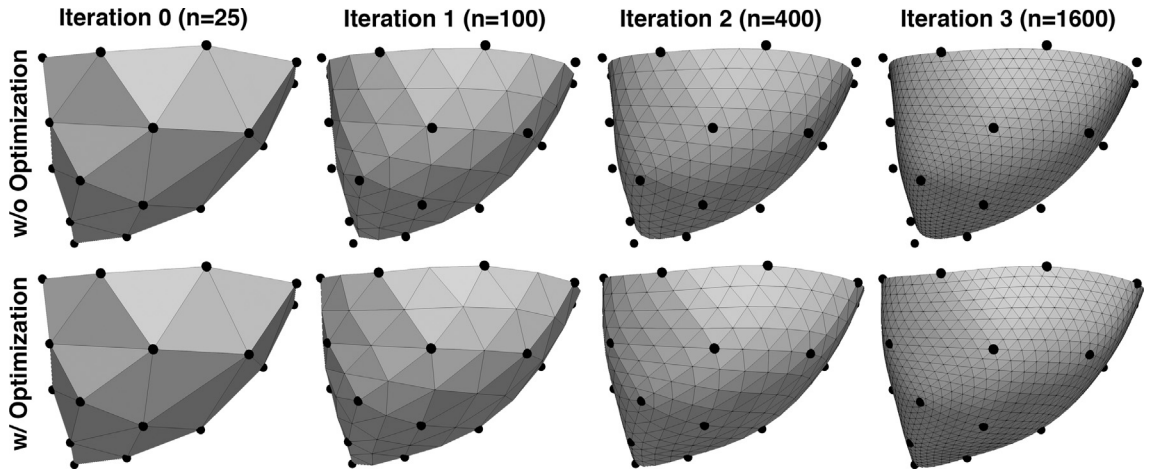

Fig. 2. Subdivision iterations from a piece-wise planar surface representation of the right ventricular epicardial surface (Iteration 0) to a C^2-continuous, smooth representation of that same surface (Iteration 3). Each iteration subdivides all original triangular elements into four elements. Thus, each iteration quadruples the number of triangular elements that represent the surface. The top row presents the result for the original, non-interpolating Loop subdivision scheme, while the bottom row presents the results for an optimized algorithm that ensures that the resulting smooth surface interpolates the original crystal coordinates.

Table 1
Hemodynamic data for experimental animals presented as mean ± 1 standard deviation: Heart Rate (HR), Right Ventricular Volume (RVV), Right Ventricular Pressure (RVP), Left Ventricular Pressure (LVP), and Central Venous Pressure (CVP) at End-Diastole (ED) and End-Systole (ES).

HR (min^{-1})	101 ± 6
RVP ED (mmHg)	12 ± 4
RVP max (mmHg)	24 ± 4
RVV ED (ml)	127 ± 9
RVV ES (ml)	102 ± 8
LVP ED (mmHg)	12 ± 4
LVP max (mmHg)	107 ± 5
CVP (mmHg)	9 ± 1

Fig. 3 presents the temporal evolutions of the regional circumferential strain, E_c, longitudinal strain, E_l, and areal strain, E_a, where we chose end-diastole (ED) as the reference configuration. With the exception of region 7 (apical), regional circumferential strains are negative throughout most of the cardiac cycle, with a brief positive deflection immediately after ED. While there are strong regional variations, most regional strains are largest (by magnitude) immediately following end-isovolumic relaxation (EIVR). The largest circumferential strains, by magnitude, are found on the anterior wall in regions 4 and 6.

Regional longitudinal strains show a similar temporal and spatial behavior as circumferential strains. However, longitudinal strains are larger in magnitude than circumferential strains in all regions.

Areal strains combine changes in circumferential and longitudinal directions and thus represent the directionally-independent, total deformation. Qualitatively, areal strains behave similarly to circumferential and longitudinal strains in that they are negative for most of the cardiac cycle following a brief positive deflection after ED. Also, peak areal strains occur in most regions immediately after EIVR. Interestingly, the largest areal strains (by magnitude) occur in regions 3 and 4, which are on the posterior and anterior wall, respectively, approximately halfway between base and apex.

Table 2 summarizes the between-animal averaged peak compressive circumferential, longitudinal, and areal strains. These data reflect the average of the peaks irrespective of time of occurrence, rather than the peak of the average as observed in Fig. 3. We find that average peak compressive strains vary by region between −3.34% (region 5) and −8.29% (region 4) in circumferential direction, −4.02% (region 6) and −10.57% (region 1) in longitudinal direction, and −11.07% (region 6) and −24.48% (region 3) in area. Additionally, Table 3 summarizes the average times to peak compressive circumferential, longitudinal, and areal strains. Again, these data are complimentary to Fig. 3 in that they provide the average time to peak compressive strain, rather than the time to the peak of the average compressive strain. Specifically, peak compressive strains occur approximately within one standard deviation of EIVR irrespective of region, or type of strain.

Fig. 4 presents the full spatial map of circumferential strain at ED, end-isovolumic contraction (EIVC), end-systole (ES), and EIVR for each animal and the average animal. The full spatial distributions reflect regional trends in Fig. 3, with the RV epicardial surface mostly under compression (i.e., the ventricle is contracted) throughout the cardiac cycle. The only exception, the apical region, shows positive values for some portion of the cardiac cycle in two out of the four animals. The spatial distributions also illustrate the general trend toward larger circumferential strains (by magnitude) in the mid-segment of the wall between base and apex.

Fig. 5 presents the full spatial distribution of longitudinal strain at ED, EIVC, ES, and EIVR for each animal and the average animal. Generally, full spatial maps of longitudinal strain present similar distributions as circumferential strain. A notable difference between circumferential and longitudinal strain distributions are the predominantly positive strains at EIVC in the latter and markedly positive strains at EIVC, ES, and EIVR close to the base. Overall, qualitatively and quantitatively, spatial distributions of circumferential and longitudinal strains are well-aligned with the regional analysis.

The supplemental videos (Online Resources 1 and 2) depict spatial and temporal patterns of circumferential and longitudinal strain throughout ten cardiac cycles.

4. Discussion

Quantifying RV deformation is critical to our understanding of healthy and diseased RV function. Here we developed an experimental method that allows us to resolve the spatial and temporal maps of RV epicardial strains in an ovine model. Specifically, we combined a high-density sonomicrometry crystal array spanning the entire RV free wall with a large deformation kinematics framework to elucidate the magnitudes of strains, and their spatial heterogeneities and anisotropies.

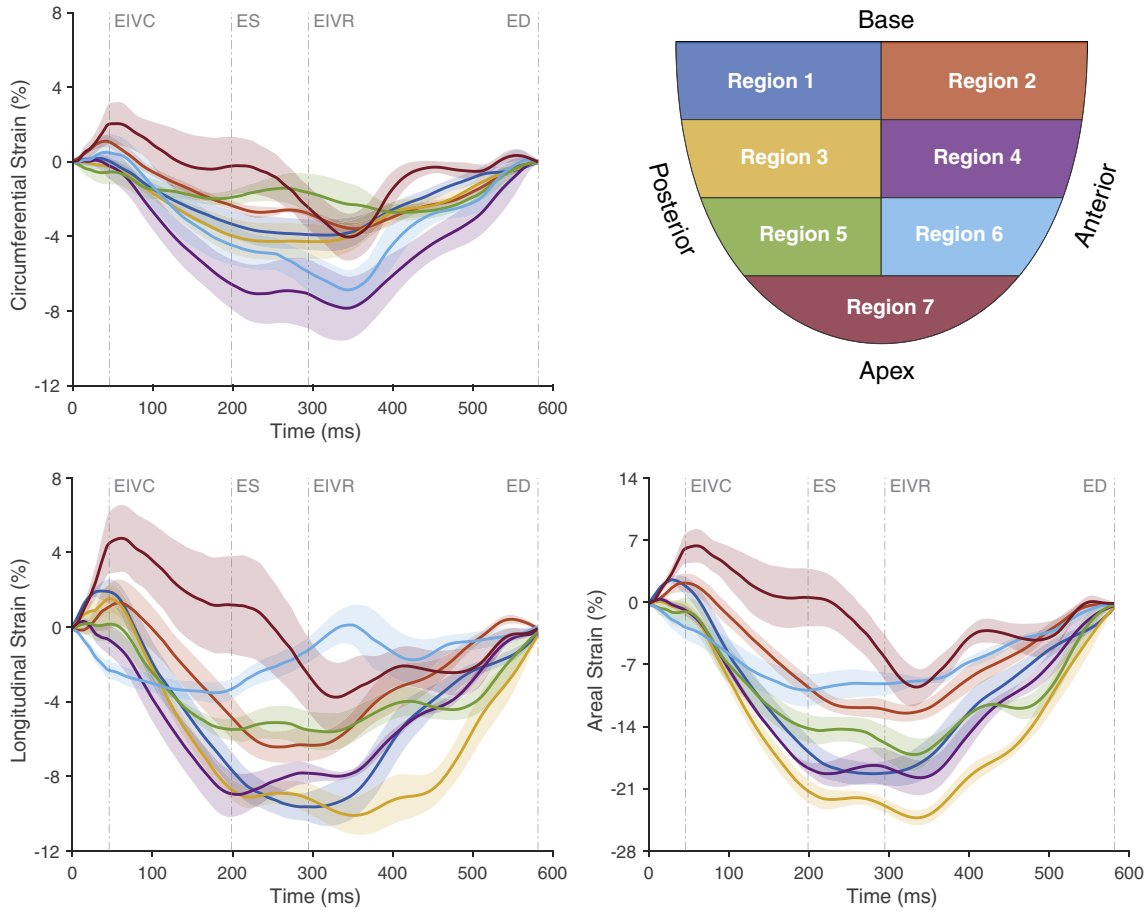

Fig. 3. Temporal evolutions of right ventricular epicardial strains with end-diastole as the reference configuration. To obtain regional right ventricular epicardial strains, we average strain values for groups of triangular elements. Specifically, we divide 25 triangular elements into seven regions and average their strain values within each region at each time point. a) Circumferential strains for all regions (mean ± 1 standard error) b) Longitudinal strains for all regions (mean ± 1 standard error), c) Areal strains for all regions (mean ± 1 standard error): End-Isovolumic Contraction (EIVC), End-Systole (ES), End-Isovolumic Relaxation (EIVR), End-Diastole (ED).

Table 2
Average peak compressive circumferential ($E_{c\ \min}$), longitudinal ($E_{l\ \min}$), and areal ($E_{a\ \min}$) strain for each region ± 1 Standard Deviation (Std.).

	Region	1	2	3	4	5	6	7
$E_{c\ \min}$ (%)	Mean	−4.10	−3.69	−4.41	−8.29	−3.34	−7.58	−4.69
	±Std.	1.86	0.77	2.24	3.52	1.48	1.93	2.83
$E_{l\ \min}$ (%)	Mean	−10.57	−6.55	−10.53	−9.60	−6.27	−4.02	−4.58
	±Std.	1.47	1.85	1.72	2.14	1.82	1.66	3.86
$E_{a\ \min}$ (%)	Mean	−20.43	−12.80	−24.48	−20.57	−17.42	−11.07	−11.31
	±Std.	2.11	2.00	1.75	3.20	4.28	2.73	3.07

Table 3
Average times to peak compressive circumferential ($t_{c\ \min}$), longitudinal ($t_{l\ \min}$), and areal ($t_{a\ \min}$) strain for each region ± 1 Standard Deviation (Std.).

	Region	1	2	3	4	5	6	7
$t_{c\ \min}$ (ms)	Mean	322	330	283	309	334	307	326
	± Std.	32	64	77	69	100	79	113
$t_{l\ \min}$ (ms)	Mean	311	297	338	281	266	217	396
	± Std.	73	57	81	79	65	145	68
$t_{a\ \min}$ (ms)	Mean	295	309	348	289	322	270	367
	± Std.	73	65	34	90	42	88	57

4.1. Comparison to previous measurements

Sonomicrometry crystals are considered the gold-standard for quantifying LV or RV deformations. Therefore, we first compare our results to previously published data on sonomicrometry crystal-derived strains. Of those studies, to the best of our knowledge, none employed more than a few crystals and usually only pairs of two. Thus, our study is the first to make use of a high-density array and the first to provide access to full spatial distributions of strains across the entire RV epicardial surface based on sonomicrometry.

Zhang et al. reported circumferential and longitudinal RV epicardial strains based on an array of three sonomicrometry crystals placed on the RV basal free wall (Zhang et al., 2013). Their reported

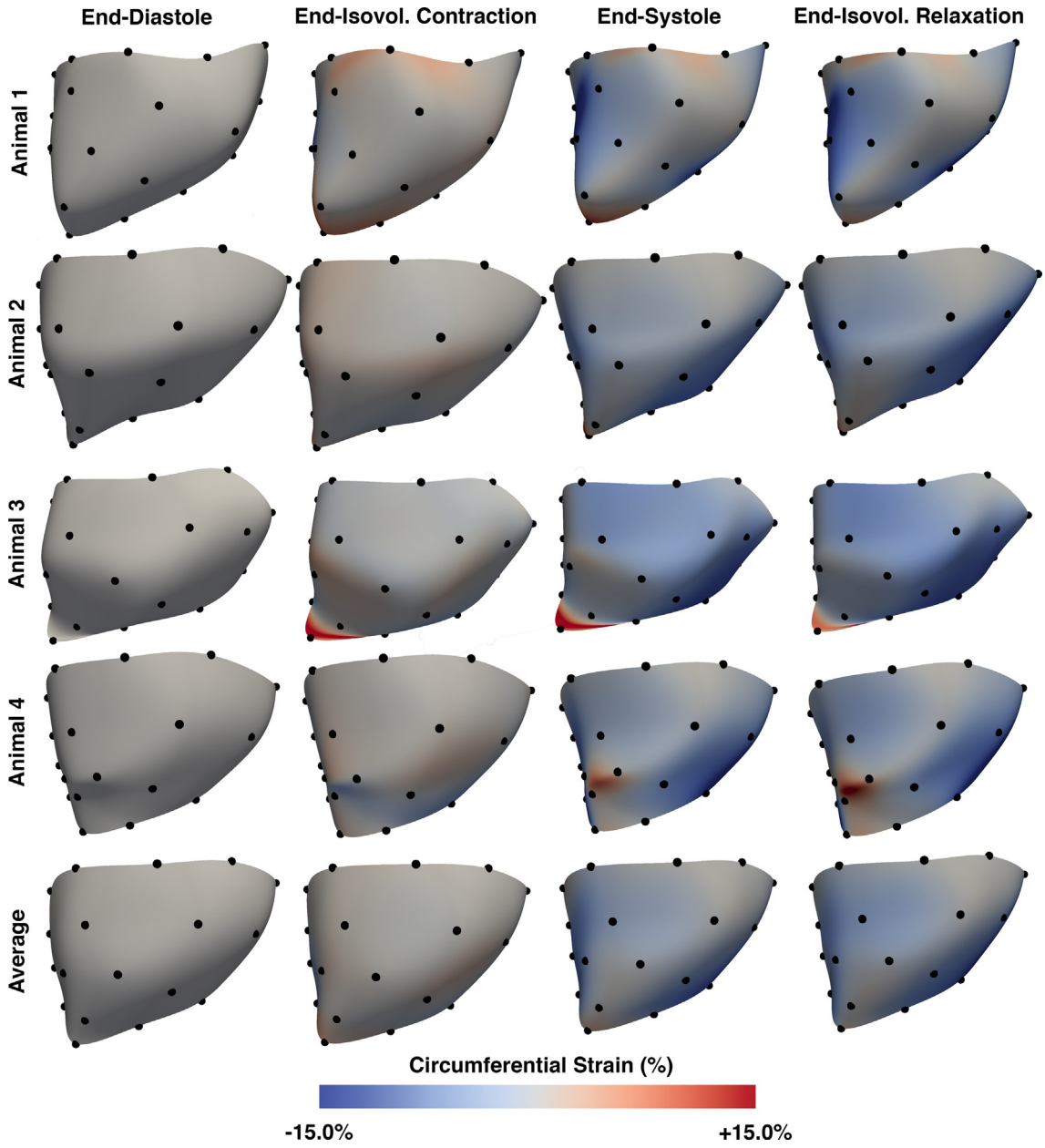

Fig. 4. Circumferential right ventricular epicardial strain maps of four animals and the average animal at four time points, relative to end-diastole. To compute strains across the smooth, interpolating, right ventricular epicardial surface, we apply the methods detailed in Section 2.2 to the subdivided triangles rather than the original, piecewise planar surface. Red indicates positive strains, meaning that the right ventricular epicardium expands locally in the circumferential direction relative to end-diastole. Blue indicates negative strains, meaning that the right ventricular epicardium contracts locally in the circumferential direction relative to end-diastole. (For interpretation of the references to color in this figure legend, the reader is referred to the web version of this article.)

temporal evolutions of circumferential and longitudinal strains fit our data qualitatively very well. Moreover, the magnitude of their reported peak strains of approximately 11% and 13% in the circumferential and longitudinal directions reflect our longitudinal strain in the basal region (approximately 10%), while deviating from our findings in the circumferential direction (approximately 4%). It is important to note that Zhang et al. report sonomicrometry-derived strain estimates in the basal region of the RV based on crystal *pairs* only. Thus, their strains reflect local effects in comparison to our values, which span a larger segment of the RV base. Additionally, Zhang et al.'s study was performed on pigs, while ours was performed on sheep.

Sonomicrometry-derived strains in the RV were also reported by Jamal et al. (Jamal et al., 2003). Qualitatively, their findings compare well with ours, while they compare quantitatively less favorably with our data (they report a magnitude of peak longitudinal strains of 17%). However, their crystals were implanted within the myocardium as opposed to on top of the epicardium as in our case.

In the same study as above, Zhang et al. performed a RV strain analysis from three-dimensional echocardiography using temporally diffeomorphic motion estimation. Their regional RV epicardial strain analysis shows very similar results to ours with values ranging by region from −2.6 to −8.1% in the circumferential direction and −5.3 to −10.4% in the longitudinal direction.

4.2. Patterns of right ventricular contraction

We found that circumferential strains and longitudinal strains (and consequently areal strains) were largest in magnitude in the

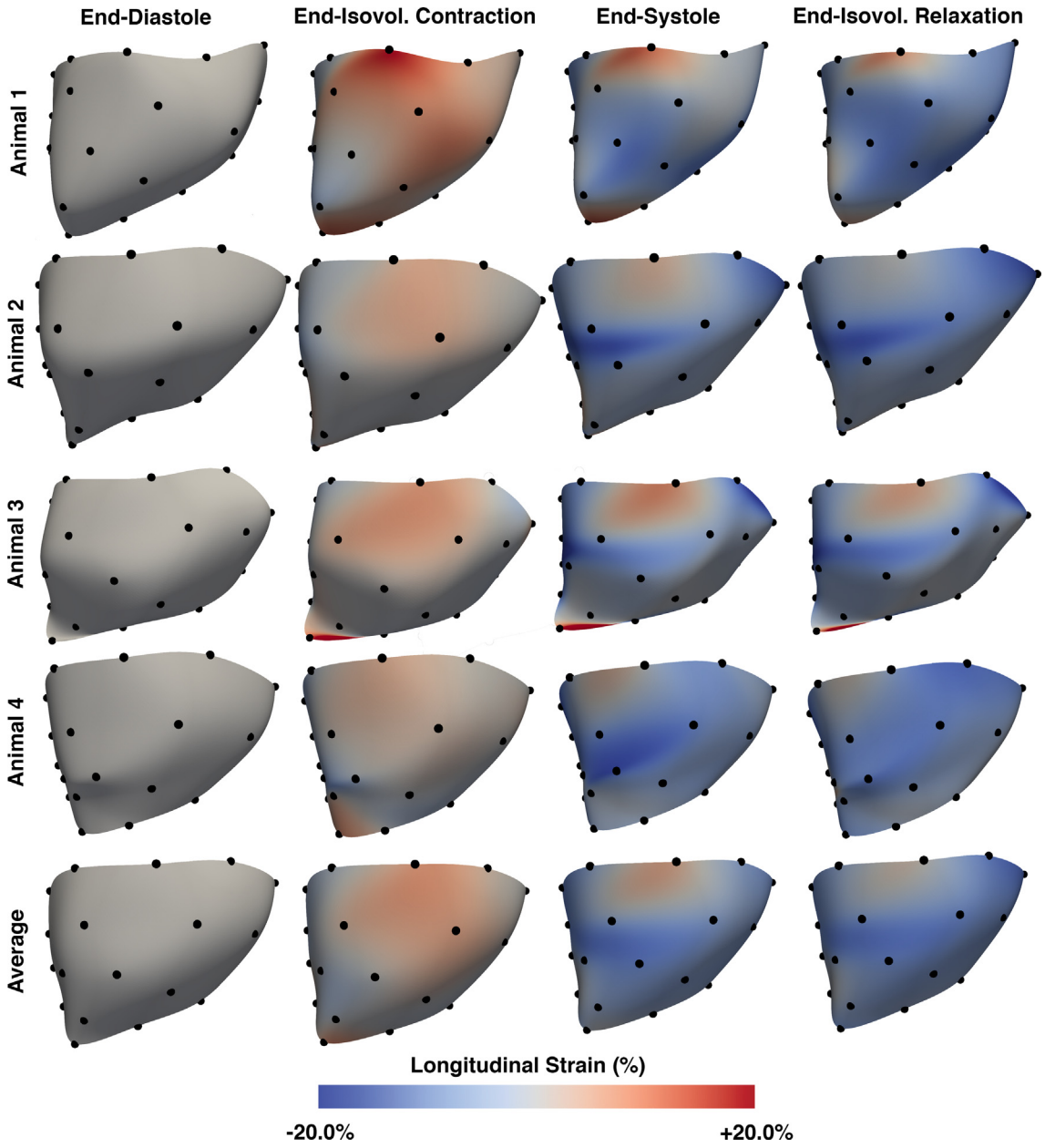

Fig. 5. Longitudinal right ventricular epicardial strain maps of four animals and the average animal at four time points, relative to end-diastole. To compute strains across the smooth, interpolating, right ventricular epicardial surface, we apply the methods detailed in Section 2.2 to the subdivided triangles rather than the original, piecewise planar surface. Red indicates positive strains, meaning that the right ventricular epicardium expands locally in the longitudinal direction relative to end-diastole. Blue indicates negative strains, meaning that the right ventricular epicardium contracts locally in the longitudinal direction relative to end-diastole. (For interpretation of the references to color in this figure legend, the reader is referred to the web version of this article.)

mid-section between base and apex. We believe strain maxima may be found in this segment as it is the least constrained. For example, in contrast to the mid-section, the free motion of the base is constrained by the mechanical coupling between RV and right atrium. Additionally, the tissue between RV and right atrium is more collagenous and less muscular, thus additionally limiting the contractility of the tissue (Haddad et al., 2008).

Moreover, we observed that longitudinal epicardial strains are larger than circumferential strains. Dominance of longitudinal strains, despite a myocyte orientation at the epicardium predominantly in circumferential direction, runs counter to a direct correlation between myocyte orientation and direction of contractile patterns. This disagreement may be due to a dominance of the muscle bulk, whose orientation deviates from circumferential and may also reveal a significant role of mechanical boundary conditions due to ventricular interdependence, for example (Hsu et al., 1998).

Finally, we also observed in our study that time-to-peak strain appeared early in the RV, when compared to findings in the LV. This observation has been made previously and may be related to the differing embryogenic origin of the RV and LV myocardium and the RV's anatomic proximity to the sinoatrial node (Addetia et al., 2016; Marcus et al., 2008).

4.3. Limitations

Among other limitations, all sonomicrometry and hemodynamic data were acquired in open-chest animals with open

pericardium and under anesthesia. RV epicardial strain measurements reported here may therefore deviate from strains under closed chest, closed pericardium, conscious conditions. Moreover, we surgically attached sonomicrometry crystals to the RV. Their weight and wire attachments may further affect kinematic data.

5. Conclusion

In this work, we present the first high-density sonomicrometry crystal array-based method for quantifying heterogeneous and anisotropic RV epicardial strains in a sheep model. We show that we are able to transform sonomicrometry-based crystal data into continuous deformation fields that encode the magnitude of strains and their directions. By means of our new methodology, we observe in four animals that RV epicardial strains vary throughout the cardiac cycle, are heterogeneous across the RV free wall, and are anisotropic with larger compressive strains, i.e., contraction, in the longitudinal direction than in the circumferential direction. In the future, we will use this method to evaluate the acute and chronic effects of disease and surgical treatment on RV kinematics.

Acknowledgements

This study was supported by an internal grant from the Meijer Heart and Vascular Institute at Spectrum Health.

Disclosures

The authors have no conflicts of interest to disclose.

Appendix A. Supplementary material

Supplementary data associated with this article can be found, in the online version, at https://doi.org/10.1016/j.jbiomech.2018.08.036.

References

Addetia, K., Takeuchi, M., Maffessanti, F., Nagata, Y., Hamilton, J., Mor-Avi, V., Lang, R.M., 2016. Simultaneous longitudinal strain in all 4 cardiac chambers: a novel method for comprehensive functional assessment of the heart. Circ. Cardiovasc. Imaging 9, 1–10. https://doi.org/10.1161/CIRCIMAGING.115.003895.

Bleeker, G.B., 2006. Assessing right ventricular function: the role of echocardiography and complementary technologies. Heart 92, i19–i26. https://doi.org/10.1136/hrt.2005.082503.

Cirak, F., Ortiz, M., Schröder, P., 2000. Subdivision surfaces: a new paradigm for thin-shell finite-element analysis. Int. J. Numer. Methods Eng. 47, 2039–2072. https://doi.org/10.1002/(SICI)1097-0207(20000430)47:12<2039::AID-NME872>3.0.CO;2-1.

Genet, M., Rausch, M.K., Lee, L.C., Choy, S., Zhao, X., Kassab, G.S., Kozerke, S., Guccione, J.M., Kuhl, E., 2015. Heterogeneous growth-induced prestrain in the heart. J. Biomech. 48, 2080–2089. https://doi.org/10.1016/j.jbiomech.2015.03.012.

Göktepe, S., Bothe, W., Kvitting, J.-P., Swanson, J.C., Ingels, N.B., Miller, D.C., Kuhl, E., 2010. Anterior mitral leaflet curvature in the beating ovine heart: A case study using videofluoroscopic markers and subdivision surfaces. Biomech. Model. Mechanobiol. 9, 281–293. https://doi.org/10.1007/s10237-009-0176-z.

Haddad, F., Hunt, S.A., Rosenthal, D.N., Murphy, D.J., 2008. Right ventricular function in cardiovascular disease, part I: Anatomy, physiology, aging, and functional assessment of the right ventricle. Circulation. https://doi.org/10.1161/CIRCULATIONAHA.107.653576.

Ho, S.Y., Nihoyannopoulos, P., 2006. Anatomy, echocardiography, and normal right ventricular dimensions. Heart 92, 2–13. https://doi.org/10.1136/hrt.2005.077875.

Hsu, E.W., Muzikant, A.L., Matulevicius, S.A., Penland, R.C., Henriquez, C.S., 1998. Magnetic resonance myocardial fiber-orientation mapping with direct histological correlation. Am. J. Physiol. 274, H1627–H1634. https://doi.org/10.1152/ajpheart.1998.274.5.H1627.

Jamal, F., Bergerot, C., Argaud, L., Loufouat, J., Ovize, M., 2003. Longitudinal strain quantitates regional right ventricular contractile function. Am. J. Physiol. - Hear. Circ. Physiol. 285, H2842–H2847. https://doi.org/10.1152/ajpheart.00218.2003.

Kroon, W., Delhaas, T., Arts, T., Bovendeerd, P., 2009. Computational modeling of volumetric soft tissue growth: Application to the cardiac left ventricle. Biomech. Model. Mechanobiol. 8, 301–309. https://doi.org/10.1007/s10237-008-0136-z.

La Gerche, A., Jurcut, R., Voigt, J.U., 2010. Right ventricular function by strain echocardiography. Curr. Opin. Cardiol. 25, 430–436. https://doi.org/10.1097/HCO.0b013e32833b5f94.

Lee, L.C., Sundnes, J., Genet, M., Wenk, J.F., Wall, S.T., 2016. An integrated electromechanical-growth heart model for simulating cardiac therapies. Biomech. Model. Mechanobiol. 15, 791–803. https://doi.org/10.1007/s10237-015-0723-8.

Lee, L.C., Wenk, J.F., Klepach, D., Zhang, Z., Saloner, D., Wallace, A.W., Ge, L., Ratcliffe, M.B., Guccione, J.M., 2011. A Novel method for quantifying in-vivo regional left ventricular myocardial contractility in the border zone of a myocardial infarction. J. Biomech. Eng. 133, 094506. https://doi.org/10.1115/1.4004995.

Loop, C., 1987. Smooth subdivision surfaces based on triangles. University of Utah, Acm Siggraph.

Malinowski, M., Wilton, P., Khaghani, A., Brown, M., Langholz, D., Hooker, V., Eberhart, L., Hooker, R.L., Timek, T.A., 2016a. The effect of acute mechanical left ventricular unloading on ovine tricuspid annular size and geometry. Interact. Cardiovasc. Thorac. Surg. 23, 391–396. https://doi.org/10.1093/icvts/ivw138.

Malinowski, M., Wilton, P., Khaghani, A., Langholz, D., Hooker, V., Eberhart, L., Hooker, R.L., Timek, T.A., 2016b. The effect of pulmonary hypertension on ovine tricuspid annular dynamics. Eur. J. Cardio-thoracic Surg. 49, 40–45. https://doi.org/10.1093/ejcts/ezv052.

Marcus, J.T., Gan, C.T.J., Zwanenburg, J.J.M., Boonstra, A., Allaart, C.P., Götte, M.J.W., Vonk-Noordegraaf, A., 2008. Interventricular mechanical asynchrony in pulmonary arterial hypertension. left-to-right delay in peak shortening is related to right ventricular overload and left ventricular underfilling. J. Am. Coll. Cardiol. 51, 750–757. https://doi.org/10.1016/j.jacc.2007.10.041.

Rausch, M.K., Bothe, W., Kvitting, J.P.E., Göktepe, S., Craig Miller, D., Kuhl, E., 2011. In vivo dynamic strains of the ovine anterior mitral valve leaflet. J. Biomech. 44, 1149–1157. https://doi.org/10.1016/j.jbiomech.2011.01.020.

Rausch, M.K., Genet, M., Humphrey, J.D., 2017a. An augmented iterative method for identifying a stress-free reference configuration in image-based biomechanical modeling. J. Biomech. 58, 227–231. https://doi.org/10.1016/j.jbiomech.2017.04.021.

Rausch, M.K., Malinowski, M., Wilton, P., Khaghani, A., Timek, T.A., 2017b. Engineering analysis of tricuspid annular dynamics in the beating ovine heart. Ann. Biomed. Eng.

Rausch, M.K., Tibayan, F.A., Craig Miller, D., Kuhl, E., 2012. Evidence of adaptive mitral leaflet growth. J. Mech. Behav. Biomed. Mater. 15. https://doi.org/10.1016/j.jmbbm.2012.07.001.

Voelkel, N.F., Quaife, R.A., Leinwand, L.A., Barst, R.J., McGoon, M.D., Meldrum, D.R., Dupuis, J., Long, C.S., Rubin, L.J., Smart, F.W., Suzuki, Y.J., Gladwin, M., Denholm, E.M., Gail, D.B., 2006. Right ventricular function and failure: Report of a National Heart, Lung, and Blood Institute working group on cellular and molecular mechanisms of right heart failure. Circulation 114, 1883–1891. https://doi.org/10.1161/CIRCULATIONAHA.106.632208.

Yeon, S.B., Reichek, N., Tallant, B.A., Lima, J.A.C., Calhoun, L.P., Clark, N.R., Hoffman, E. A., Ho, K.K.L., Axel, L., 2001. Validation of in vivo myocardial strain measurement by magnetic resonance tagging with sonomicrometry. J. Am. Coll. Cardiol. 38, 555–561. https://doi.org/10.1016/S0735-1097(01)01397-3.

Zhang, X., Liu, Z.Q., Singh, D., Wehner, G.J., Powell, D.K., Campbell, K.S., Fornwalt, B. K., Wenk, J.F., 2017. Regional quantification of myocardial mechanics in rat using 3D cine DENSE cardiovascular magnetic resonance. NMR Biomed. 30, 1–9. https://doi.org/10.1002/nbm.3733.

Zhang, Z., Sahn, D.J., Song, X., 2013. Right ventricular strain analysis from 3D echocardiography by using temporally diffeomorphic motion estimation. Lect. Notes Comput. Sci. (including Subser. Lect. Notes Artif. Intell. Lect. Notes Bioinformatics) 7945 LNCS, 474–482. https://doi.org/10.1007/978-3-642-38899-6_56.

Zhong, X., Spottiswoode, B.S., Meyer, C.H., Kramer, C.M., Epstein, F.H., 2010. Imaging three-dimensional myocardial mechanics using navigator-gated volumetric spiral cine DENSE MRI. Magn. Reson. Med. 64, 1089–1097. https://doi.org/10.1002/mrm.22503.